Solar Probe Plus: Unique Navigation Modeling Challenges

Drew Ryan Jones[*], Troy Goodson[*], Paul Thompson[*], and Powtawche Valerino[*]
Jet Propulsion Laboratory, California Institute of Technology, Pasadena, CA 91109

Jessica Williams[†]
Lockheed Martin Space Systems Company, Sunnyvale, CA 94089

The Solar Probe Plus (SPP) mission is preparing to launch in 2018, and will directly investigate the outer atmosphere of our star. At 9.86 solar radii, SPP must operate in an unexplored regime. The environment and aspects of the mission design present some unique challenges for navigation, particularly in terms of modeling the dynamics. Non-gravitational force models, unique to this mission, are given with analytical expressions. For each of these models (and error sources), a maximum bound on the force perturbation magnitude is quantified numerically. Additionally, the effect of charged particles on radiometric observables is discussed, along with methods being employed to pre-process the measurements. This survey is an overview of unique modeling employed by SPP navigation, but also a reference for future missions traveling near the Sun.

I. Introduction

Solar Probe Plus (SPP) is a unique and historic mission, exploring what may be the final frontier in the solar system, the Sun's outer atmosphere. SPP will repeatedly sample the near-Sun environment to enhance our fundamental understanding of the corona, and the structure, origin, and evolution of the solar wind.[1] SPP will experience heliocentric speeds up to 190 km/sec, making it the fastest man-made object to date.

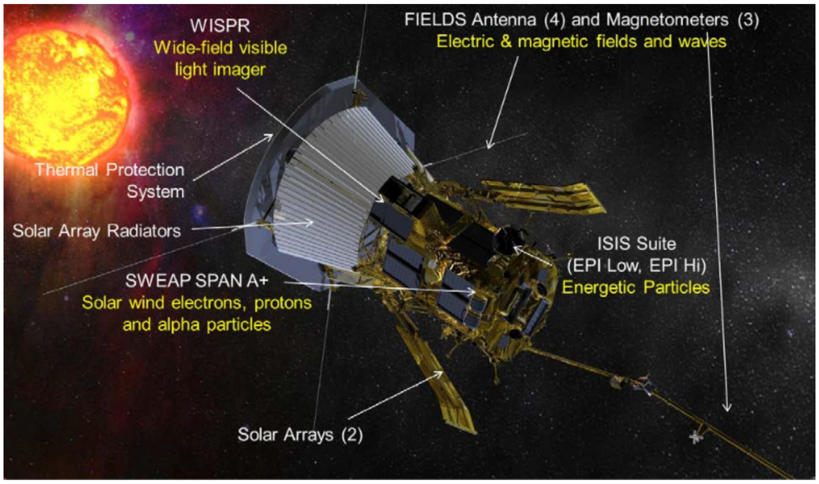

Figure 1: Solar Probe Plus spacecraft.[2]

---

[*] Mission Design and Navigation Staff, Jet Propulsion Laboratory, California Institute of Technology, 4800 Oak Grove Drive, Pasadena, California 91109.

[†] Senior Systems Engineer, Lockheed Martin Space Systems Company, 1111 Lockheed Martin Way, Sunnyvale, California 94089. *Formerly:* Jet Propulsion Laboratory, California Institute of Technology.

The spacecraft is shown in Figure 1, and is designed and built by the Applied Physics Laboratory (APL) with navigation support provided by the Jet Propulsion Laboratory (JPL). The project recently entered Phase D, with its first launch opportunity on July 31, 2018 aboard a Delta-IV Heavy. The reference trajectory design, depicted in Figure 2, uses seven Venus gravity-assist flybys to gradually reduce perihelion to 9.86 solar radii. The reference trajectory is entirely ballistic, and the total mission duration is 7 years.[2] The 20-day primary launch period permits daily launch opportunities, and a similar backup period is available in 2019. More than 40 trajectory correction maneuvers (TCM) are planned to correct errors and perturbations. Each launch opportunity has a unique reference trajectory, with variable flyby dates, TCM events, and tracking schedule constraints. Having launch opportunity specific reference missions is a challenge for pre-launch analysis and operational planning.

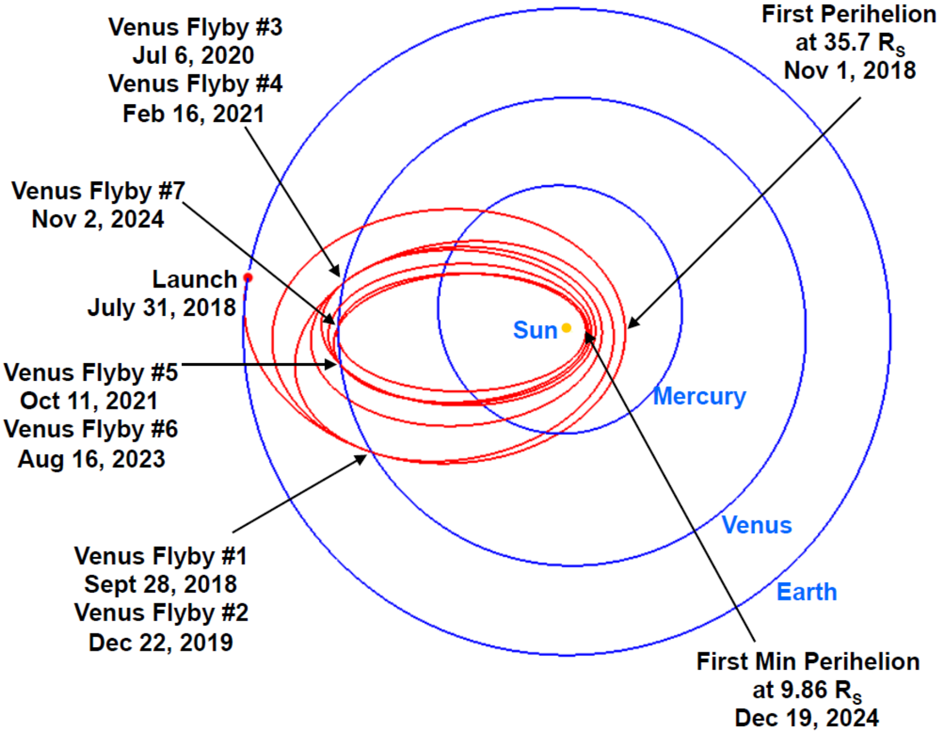

Figure 2: Reference trajectory for primary launch period open.

Some important navigation requirements include mission $\Delta V99$ (the least upper bound for the total ΔV required to control 99% of sampled dispersed trajectories), reconstructed ephemeris accuracy, and predicted ephemeris accuracy. The requirement for predicted ephemerides uncertainty varies over an orbit, becoming tightest (small) when the spacecraft solar range is below 0.25 AU. The extreme flight regime manifests a number of operational challenges for navigation. First, momentum desaturation maneuvers (desats) are performed on unbalanced thrusters, and autonomously when solar range is below 0.25 AU. Proximity to the Sun induces strong perturbations from solar radiation, thermal re-emission, and charged particles in addition to significant heating. During prime science, the perihelion distance will be almost one-seventh that of Mercury, such that the Sun is not well approximated as a point-mass source of light.

This paper identifies some navigation challenges unique to SPP. In particular, it details non-gravitational force modeling likely neglected or significantly different for other space missions. Anticipated future papers will describe orbit determination covariance analyses, TCM design strategy, and $\Delta V99$ results. This article is organized into categories of non-gravitational force, respectively described in sections III-VI. This is followed by a summary and quantification of the error sources associated with these models in section VII. Lastly, section VIII outlines errors introduced to radiometric observables by solar charged particles, as well as methods for correcting the measurements.

II. Background

The Solar Probe Plus spacecraft consists of a prominent thermal protection system (TPS), two primary solar panels, two secondary panels, an upper bus structure housing the radiators (cooling system), and a lower spacecraft bus structure (see Figure 1). The lower bus houses the magnetometer boom, twelve 4.4 N thrusters, four reaction wheels, five communication antennae, and most of the remaining vehicle components. Spacecraft coordinate frames are depicted in Figure 3. The body coordinate frame (axes x, y, z) has z along the TPS normal, x in the ram direction (towards direction of motion), and y completes the set. Additionally, an orbit frame is defined similarly with axes X, Y, Z. Where, Z is the SPP-to-Sun unit vector, Y is the angular momentum direction of SPP about the Sun, and X completes the set. For most of the mission, z and Z are approximately coincident. Figure 4 depicts the solar panel array configuration at the minimum solar distance, where each wing (side) consists of a primary and a secondary panel. The smaller secondary panel is rotated (about x) from the primary panel by a fixed 7.4 degrees, such that at minimum distance the secondary panels account for almost all of the power. Below 0.7 AU, the panel's normal directions are constrained to the y-z plane, rotated about the x axis by a flap angle θ_f. Beyond 0.7 AU, the panels may rotate about their longitudinal axis (feather angle).

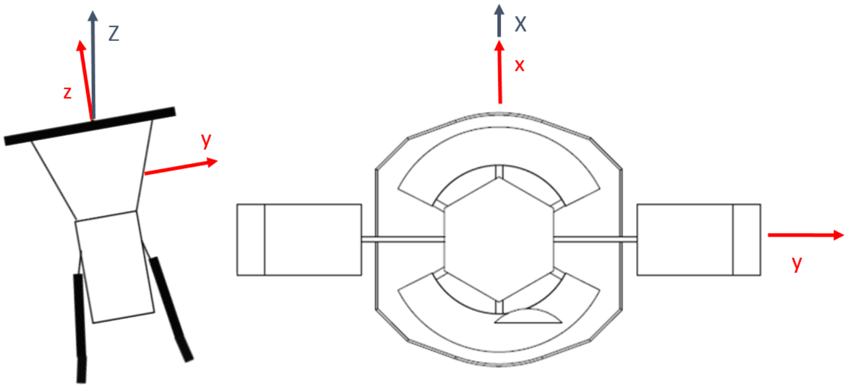

Figure 3: SPP coordinate frames diagram.

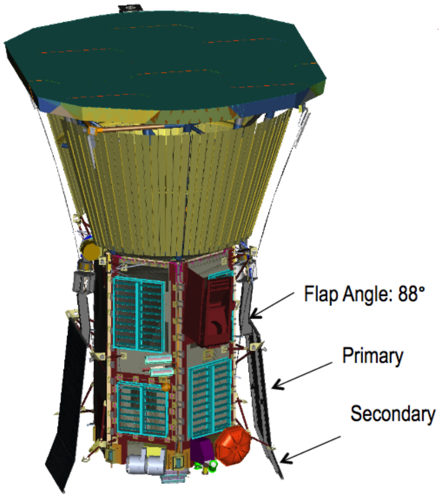

Figure 4: SPP spacecraft depicting solar panel array geometry.

The nominal attitude profile for SPP is based on solar range:

- *Sun range* $< 0.25\ AU$: z to Sun, $+x$ towards RAM. Solar panels significantly shadowed by TPS. No feather angle, flap angle is non-zero.

- *0.25 AU < Sun range < 0.7 AU*: z to Sun, rotation permitted about z. Solar panels partially shadowed. No feather angle, flap angle is non-zero.
- *0.7 AU < Sun range*: Slew about y up to 45 degrees, rotation permitted about z. Solar panels in full Sun. Feather angle permitted, flap angle is zero.

III. Solar radiation pressure

Total solar radiation pressure (SRP) is a combination of force from reflected particles, and force from particles absorbed and re-radiated (via thermal emission). Let γ denote the fraction of incoming radiation that is reflected, and η the fraction absorbed. Therefore, assuming zero transmissivity

$$\gamma + \eta = 1$$

The reflected portion γ is typically split into specular and diffuse components (describing the direction of reflection). This is quantified by the specular and diffuse coefficients, μ and ν, respectively. Furthermore, assuming a relatively short time to thermal equilibrium, re-radiated emission exerts a force equivalent to diffuse reflection. Hence, ν may be amended to include a term for the force due to re-radiated emission.

For SPP, the total SRP force is approximated as the vector sum of forces acting on a finite number of shape elements.

$$\mathbf{f}_{srp}(t) = \frac{S\ C}{r^2} \sum_{i=1}^{n} A_i\ \bar{\mathbf{f}}_i = S \sum_{i=1}^{n} \mathbf{f}_i \tag{1}$$

where S is a net scale factor that accounts for variable solar output, and r is the solar range.[*] Also, C is the average solar flux constant at 1 AU (in units of force)[†], and is derived from the solar irradiance constant by multiplying by (1 AU)^2 and dividing by the speed of light. Each shape element has corresponding reference area A, and vector $\bar{\mathbf{f}}$ (which indicates the direction of force contribution, and accounts for the area projection). Therefore $\bar{\mathbf{f}}$ is some function of incoming radiation direction and the coefficients μ and ν.

A. Shape elements

Navigation uses flat plate shape elements to model the physical vehicle and an element which allows for arbitrary (non-physical) contributions. The latter is necessary to consider unmodeled (generally non-radial) SRP errors, for example due to TPS pointing bias. The flat plate elements include:

- TPS with normal direction along z
- Primary panels (2) with normal direction generally in y-z plane
- Secondary panels (2) with normal direction generally in y-z plane
- Bus element with normal along x
- Bus element with normal along y

The general force contribution from a flat plate may be written as[3]

$$\mathbf{f}_{\text{plate}} = \frac{C\ A}{r^2}\ \bar{\mathbf{f}} = \frac{C\ A}{r^2} \left[(2\mu - 1)\cos\alpha\ \hat{u}_r - (2\nu + 4\mu\cos\alpha)\cos\alpha\ \hat{u}_n\right] \tag{2}$$

Where, $\hat{u}_r$ is the incoming light unit direction (approximate spacecraft to Sun direction), $\hat{u}_n$ is the unit direction normal to the plate, and α is the angle between $\hat{u}_n$ and $\hat{u}_r$.

Due to the significant amount of thermal emission (re-radiation out the front), the TPS is best approximated as a perfectly diffuse reflector ($\mu = 0$ and $\nu = 1/3$). This differs from the body's optical properties. Therefore, the TPS SRP force is given as

$$\mathbf{f}_{\text{tps}} = -\frac{C\ A_t}{r^2} \left[\hat{u}_r + 2/3\,\hat{u}_n\right]\cos\alpha = \begin{bmatrix} f_r \hat{u}_r \\ f_n \hat{u}_n \end{bmatrix} \tag{3}$$

---

[*] In general, all parameters may be a function of time, but for brevity the t dependence is omitted in what follows.

[†] C is approximately 101.979E12 kg km/s^2 (using a solar irradiance at 1 AU of 1366 W/m^2)

In addition, a so-called S/C-bus element is added to account for various sources of non-radial SRP acceleration, not necessarily associated with the actual spacecraft bus. This element is non-physical, but can be used to correct for physical accelerations due to asymmetric thermal re-radiation, TPS alignment error and attitude error, asymmetric solar panels, etc. The contribution is given by Eq. (4), and the body frame is assumed.

$$\mathbf{f}_{\text{sc-bus}} = \frac{C\ A_{\text{bus}}}{r^2} \begin{bmatrix} G_x \\ G_y \\ G_z \end{bmatrix} \tag{4}$$

The parameter G_z reflects a (generally) radial contribution and is set to 0 (not estimated). The parameters G_x and G_y are nominally zero, but may attain non-zero a priori values during operations. These parameters may be estimated as stochastic (time-series valued). The area for this shape is notionally set as $A_{\text{bus}} = (A_t/3)\ 0.07\% = 0.00104\ \text{m}^2$, based on analysis bounding the various sources of non-radial SRP acceleration[4], such that an expected 1-σ error yields $G_x = G_y = 1$. Coefficients and nominal areas for all shape elements are listed in table 1.

Table 1: SRP shape model parameters

Element	Area	μ	ν
TPS	4.474 m^2	0	1/3
Primary panel (2)	0.601 m^2	0.0	0.0023
Secondary panel (2)	0.175 m^2	0.0	0.0023
Bus plate x	3.29 m^2	0.12	0.083
Bus plate y	2.72 m^2	0.12	0.083
S/C Bus	0.00104 m^2	-	-

Generally, any of the area parameters may be estimated, while the reflectivity coefficients are kept constant. The overall scale factor S is also estimated. Areas listed for the solar panels do not consider shadowing, and during the critical time below 0.25 AU, most of the panel area is in shadow.

B. Solar panel shadowing

In Ref. 5, a finite-element shadowing model is presented for SPP. This high-fidelity approach determines whether a differential element of panel is in full sun, partial sun (penumbra) or shadow (umbra), and also accounts for solar limb darkening. Navigation approximates these effects more coarsely, in part so as to not significantly increase integration time. Effectively, the shape element areas are scaled down based on how much of the panel is in shadow.

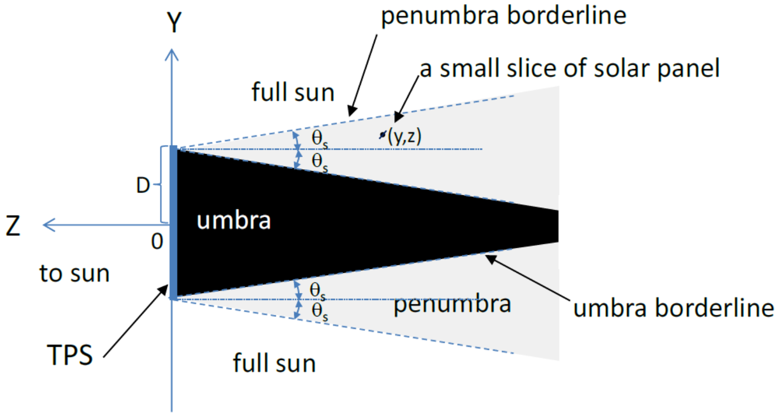

Figure 5: Solar panel shadowing geometry.[5]

The shadowing geometry is depicted by Figure 5, where the shadow angle θ_s is a function of the Sun's radius R_s and the solar range r

$$\theta_s = \sin^{-1}\left(\frac{R_s}{r}\right) \tag{5}$$

Below 0.7 AU, there is only one degree of freedom for the panels, a rotation about x referred to as the flap angle θ_f. Therefore, for most of the mission (and when SRP has the most significant effect), the element normal directions ($\hat{u}_n$ in Eq. (2)) are defined by θ_f. For the purposes of shadowing computations, the feather angle is not considered.

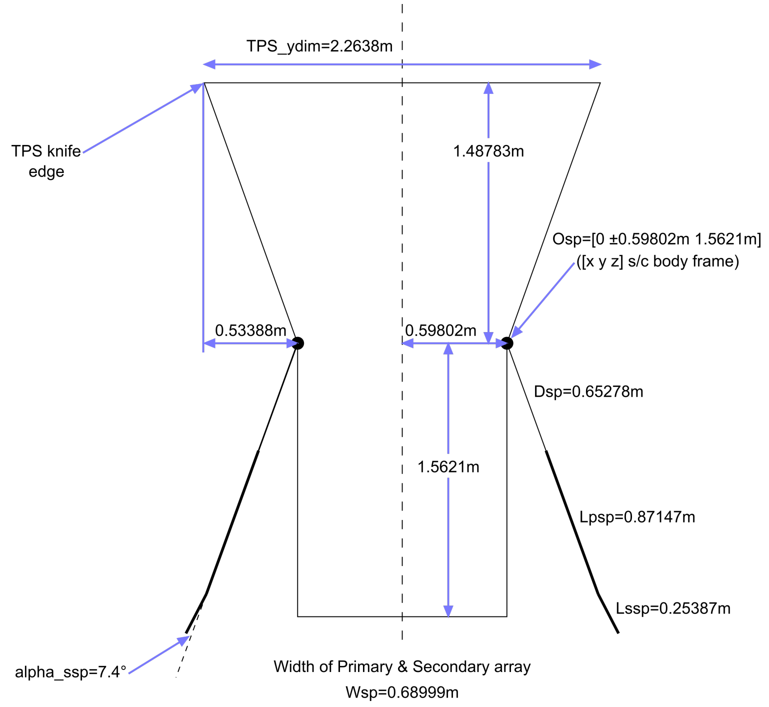

Figure 6: Solar panel geometry with dimensions.[5]

A schematic of the solar panel geometry (with dimensions) is shown in Figure 6. Based entirely on the geometry, equations may be derived indicating the penumbra and umbra intersection points as a function of θ_s and θ_f (each itself a function of solar distance). The intersections may be written parametrically as a distance along a solar panel element length. Consider a panel element with length l and reference area A. Let d_u indicate the distance along the length of the element where the umbra intersection occurs, and d_p where the penumbra intersection occurs. For the primary panel elements, the distances are given by

$$d_u = \frac{0.534\text{m} - 1.48783\text{m} \tan\theta_f}{\cos\theta_f + \sin\theta_f \tan\theta_s} \qquad d_p = \frac{0.534\text{m} + 1.48783\text{m} \tan\theta_f}{\cos\theta_f - \sin\theta_f \tan\theta_s} \tag{6}$$

Boundary conditions must be enforced on Eq. (6) to ensure the distances are between the minimum and maximum distance (from the attachment point). Exceeding those bounds indicates the element is in full shadow or full sun. Similar expressions may be derived for the secondary panel elements, while adjusting for the 7.4 degree rotation. With d_u and d_p known, the percent area in full sun, percent area in penumbra, and percent area in umbra (for that element) are

$$A_s = \frac{l - d_p}{l} \qquad A_p = \frac{d_p - d_u}{l} \qquad A_u = \frac{d_u}{l} \tag{7}$$

With d_u and d_p modulated to be between 0 and l. The effective area can be approximated as

$$A_{\text{effective}} = A\left(A_s + \xi A_p\right) \tag{8}$$

where ξ is a number between 0 and 1, and specifies the average fraction of irradiance in the penumbra.

Discrete effective areas (for all four solar panels shape elements) may be precomputed from a reference trajectory and flap angle history.[‡] These area time histories may then be used as the nominal values for A in Eq. (2), when computing SRP acceleration.

Note, this approximation does not account for solar limb darkening (i.e. the fact that there is more irradiance in the penumbra region further from the spacecraft bus, and less irradiance closer to the umbra). Equation (8) implies the penumbra irradiance is constant, but less than that of full sun. Ref. 5 provides a series expansion approximation for the irradiance in the penumbra as a function of solar range and geometric location with respect to the TPS edge. It is estimated that neglecting solar limb darkening could yield a perturbation as high as 10 μN. Methods for modeling the effect, without incurring the substantial integration performance penalty inherent to finite element approaches, are currently being investigated.

C. Aberration of incoming light

Aberration of light is an apparent rotation of the incoming light direction, relative to a moving reference frame. The light source appears rotated towards the direction of motion. For SPP, the direction of incident solar radiation is rotated from the Sun-spacecraft (radial) direction by an angle proportional to the speed of the spacecraft. The fundamental geometry is depicted in Figure 7. The light velocity vector relative to Sun $\mathbf{u}$ is along the Sun-spacecraft line, and $\mathbf{u}'$ is the light vector relative to the spacecraft, which is traveling with velocity $\mathbf{v}$ (relative to the Sun). The 'relativistic transformation of velocities' is given by Eqs. (9a)-(9b), with components along the $\hat{t}$ and $\hat{s}$ directions[6]

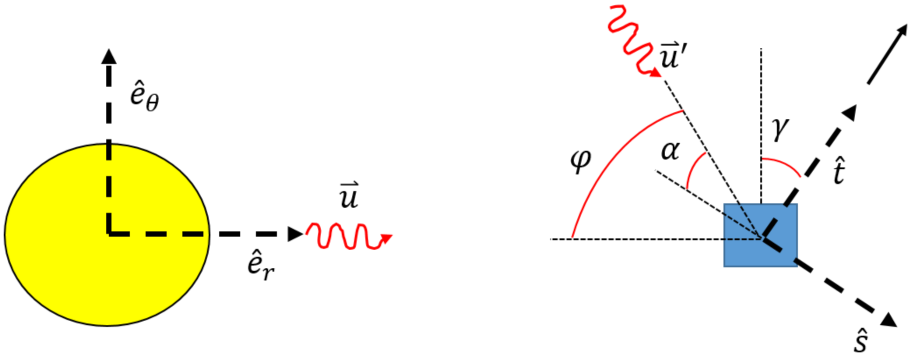

Figure 7: Geometry of incident light aberration.

$$u'_t = \frac{u_t - v}{\left(1 - \frac{u_t v}{c^2}\right)} = \frac{c\sin\gamma - v}{\left(1 - \frac{v\sin\gamma}{c}\right)} \tag{9a}$$

$$u'_s = \frac{u_s}{\Gamma\left(1 - \frac{u_t v}{c^2}\right)} = \frac{c\cos\gamma\sqrt{1 - \frac{v^2}{c^2}}}{\left(1 - \frac{v\sin\gamma}{c}\right)} \tag{9b}$$

where γ is the flight path angle, and Γ the relativistic correction term, ensuring c is conserved in all frames.

SPP's speed is high enough for the incoming light direction rotation to be non-negligible, but low enough that relativistic terms may be neglected. At the maximum speed of 190 km/sec we have $\Gamma - 1 = 2.0$E-7. Hence, the incoming radiation direction ($\hat{u}_r$) may be approximated using classical vector addition.

$$\hat{u}_r = -\hat{u'} = \frac{\mathbf{v} - c\hat{u}}{\|\mathbf{v} - c\hat{u}\|} \tag{10}$$

This approximation (which does not conserve c) is implemented in the operational Navigation software MONTE, and the effect may be toggled on/off. With aberration included, the incoming light direction $\hat{u}_r$ of Eq. (2) is not exactly equal to the spacecraft-Sun direction ($-\hat{u}$).

[‡] The flap angle is approximated by a power series in r.

IV. Momentum Desaturation Maneuvers

During the critical time spent below 0.25 AU, momentum desaturation maneuvers (desats) are autonomous with uncertain frequency. Additionally, much of the time spent below 0.25 AU occurs without tracking data (or with substantial data gaps). Each desat produces a residual ΔV (with associated uncertainty). Table 2 provides current best estimate nominal and standard deviation values for momentum dump ΔV based on G&C Monte-Carlo analyses. These statistics do not include variations in momentum threshold (since that will be known prior to launch), or fuel level. The latter has been analyzed[4] and accounts for a ΔV uncertainty of less than 10%.

Table 2: CBE nominal momentum dump residual ΔV in the body frame

	x, mm/s	y, mm/s	z, mm/s
Mean	1.5	0.0	9.6
Standard Deviation	2.3	0.6	1.7

A. Correlated desat ΔV error

Individual desat ΔV errors have the worst effect, in terms of predicted spacecraft state uncertainty, if the error is biased (or correlated). Although unlikely, if this error is unresolved by the time of the final three orbits (where as many as 20 events can occur during single perihelion), the accumulated error can be quite large. A bound for this error is quantified by perfectly correlating the standard deviation errors from Table 2. For 20 desat events, the error bound is 6.57 mm/sec/day. For a mass of 665 kg, this yields an average perturbation (over a single 0.25 AU pass) of 51 μN.

B. Frequency uncertainty

The frequency is proportional to the momentum dump threshold and accumulated SRP torque. The former will be known prior to launch, but the latter is an uncertain function of Cp-Cg offset, solar activity (random), and attitude errors (mostly random). The SPP G&C team provides a notional desat schedule (implying a nominal frequency), and navigation must account not just for the single-event maneuver errors but also for considerable uncertainty in the number of events.

For pre-launch analyses and early in the operational mission, frequency uncertainty is assumed to be the resulting frequency difference between nominal and worst-case Cp-Cg offsets (3-σ). This uncertainty is applied as a biased (or correlated) ΔV offset upon all notional desats in a given arc. This level of ΔV uncertainty is overly conservative later in the mission, because once navigation and G&C teams are able to observe the number of desats for some number of perihelion passes, the frequency uncertainty can be reduced.

V. Plasma Drag

The solar wind consists of high energy plasma particles, released from the upper atmosphere, which travel outward (mostly radially) at high speed. The plasma particles impact the spacecraft and impart momentum (a drag force). Since the velocity of the spacecraft and the plasma define the relative velocity, the force has both radial and along-track components The solar wind is modeled as expanding spherically[§], such that

$$\rho v_p r^2 = \text{constant} \tag{11}$$

Where ρ and v_p are the density and radial speed of plasma, respectively, and r the solar distance. On average, density and speed scale with r such that[§]

$$\rho(r) = \rho_0 \left(\frac{r_0}{r}\right)^{2.2} \tag{12}$$

[§] Email correspondence (June-September, 2016) with Dr. Justin Kasper, P.I. SWEAP investigation on SPP and Associate Professor at the University of Michigan Ann-Arbor.

$$v_p(r) = v_0 \left(\frac{r}{r_0}\right)^{0.2} \tag{13}$$

ρ_0 and v_0 are the density and plasma speed, respectively at r_0 =1 AU. From Refs. 8,9 $\rho_0 = 1.6\text{e-}11$ kg/km^3 is assumed, and from Refs. 10,9 $v_0 = 500 \pm 300$ km/sec is assumed.[¶] The drag force is then

$$\mathbf{f}_d = \frac{c_d \rho \ v_{\text{rel}}^2}{2} \sum_{i=1}^{n} A_i^d \hat{n}_i \hat{v}_{\text{rel}} \tag{14}$$

where c_d is the ballistic coefficient of drag, and A_i^d is a flat plate area with normal direction $\hat{n}_i$, and $\mathbf{v}_{\text{rel}}$ is the incoming plasma velocity vector. The incoming velocity vector is the difference between the inertial spacecraft velocity $\mathbf{v}$ and the inertial plasma velocity $\mathbf{v}_p$ (plasma has negligible non-radial component). The summation in Eq. (14) is over the shape element areas projected along the incoming plasma direction.

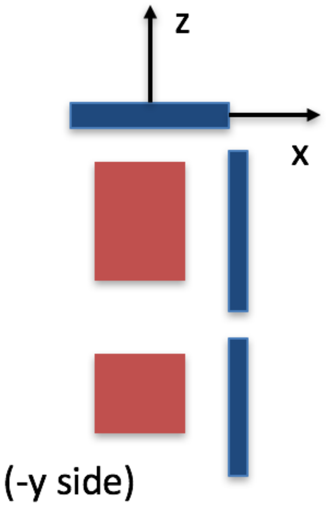

Figure 8: SPP shape model elements for plasma drag calculation.

Similar to the formulation for SRP, the spacecraft shape used for the drag computation is defined to consist of a finite number of flat plate elements. Figure 8 shows how the shape is approximated for the purposes of drag computations. A total of three elements are used, with normal directions along each of the body frame axes. From vehicle assembly drawings, the elements and their projected areas (projections onto a body axis) are as follows:

- **TPS:** Aligned with z, and having nominal area $A_1^d = 4.574$ m^2.
- **x-bus:** Along x with $A_2^d = 3.29$ m^2 (combined lower and upper bus areas of 1.510 m^2 and 1.780 m^2, respectively)
- **y-bus:** Along y with $A_3^d = 2.72$ m^2 (combined lower and upper bus areas of 1.743 m^2 and 0.979 m^2, respectively)

VI. Other Forces Considered

For this unique mission, some additional forces were quantified and deemed small enough to neglect from a navigation perspective. These include the Lorentz force, outgassing, thermal re-radiation (via solar array cooling system), and Venus atmospheric drag. The following summarizes analyses performed to bound the potential biased error, due to disregarding each model.

[¶] The speed uncertainty is conservative, to partially account for the lack of attributed uncertainty in ρ_0.

A. Lorentz force

The Lorentz force applies to a charged body moving through an external magnetic field. For SPP, the charged spacecraft is moving relative to the Sun's magnetic field. The force is

$$\mathbf{f}_q = q\,(\mathbf{v} \times \mathbf{B}) \tag{15}$$

Where q is the net charge, $\mathbf{v}$ the spacecraft velocity relative to the magnetic field $\mathbf{B}$. Conservatively, the maximum possible force magnitude is quantified. This occurs when $\mathbf{v} \perp \mathbf{B}$ such that $f_q = qvB$. The electric potential of the spacecraft V_{sc} (relative to ambient), may be related to q, by assuming a control volume of radius R_{cv}

$$V_{\text{sc}} = \frac{k_c\, q}{R_{cv}} \tag{16}$$

Where k_c is the Coulomb constant. The spacecraft will accumulate its maximum surface potential of around +6.3 V, at the 0.25 AU boundary.[‖] This equates to a net charge of around 1.0E-9 C. In Ref. 11, a power law is fit to the solar magnetic field strength versus distance, based on empirical data. This law has the field decreasing from 48 to 8 mG in the range 6 to 23 solar radii. Substituting the overly conservative values of 1.0E-9 C and 48 mG for q and B into Eq. (15) (at the max SPP speed), yields a force of only 1.0E-9 N. Therefore, the Lorentz force is reasonably neglected.

B. Outgassing

The phenomenon of outgassing occurs just after launch for all space missions. As spacecraft surfaces are exposed to the Sun, ice-water and other elements are expelled as gas, creating a force which typically decays exponentially. Navigation typically models this with a three-axis acceleration decaying with a time constant on the order of days. Based on data from Mars Reconaissance Orbiter and Mars Science Laboratory, the acceleration may be bounded conservatively on the order of 1.0E-10 km/sec^2. This will be important just after launch, but unnecessary thereafter.

C. Thermal re-radiation from cooling system

SPP employs a sophisticated cooling system, where heat energy is expelled via radiators along the bus. The radiator locations are depicted in Figure 9, and the radiation flux direction is mostly non-radial (with some component in the negative body z direction). The heat input to the cooling system is dependent on solar array operations and spacecraft attitude, in addition to solar range. The nominal heat energy input thereby varies over the mission, but does not follow a $1/r^2$ law (unlike SRP), and peaks at around 4500 W.

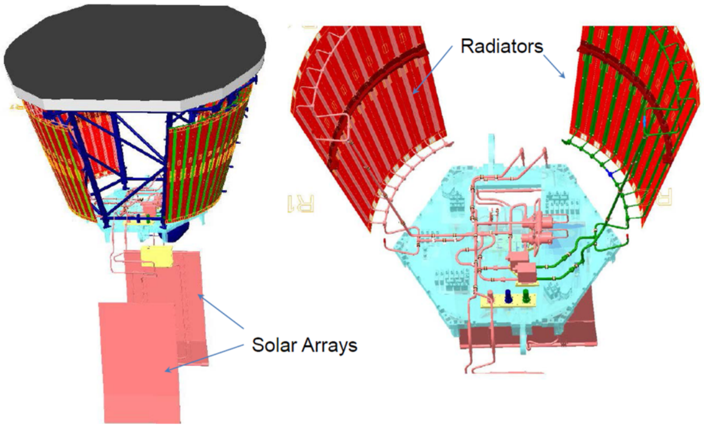

Figure 9: Radiator location diagram.

The net force from the radiators is

$$\mathbf{f}_{\text{radiate}} = \frac{1}{4} \sum_{i=1} \frac{E\, \mathbf{d}_i}{c} \tag{17}$$

[‖] From "Spacecraft Surface Charging" presentation at the SPP Preliminary Design Review (January 2014).

where **d** is a normal direction for each of the four radiators, E the net heat energy, and c the speed of light. From Figure 9, it is clear that the force in the x-y plane will nominally cancel. The cancellation assumes the four radiators emit heat equally, but Ref. 4 bounds the amount of non-radial force from radiator asymmetries. This is found to be 0.096 μN, using expected uncertainties in radiator imbalance at the peak heating load.

Although the net force in the z direction is more significant, it is left unmodeled since it is still many orders of magnitude less than SRP force uncertainties (which also perturb along z). In practice, the error will be accounted for by estimating other parameters (such as plate areas and overall SRP scale factor).

D. Atmospheric drag at Venus

Although modeling atmospheric drag is common place for orbiters, it is an unexpected force for a mission consisting of relatively high-altitude flybys. The minimum Venus flyby altitude for SPP is around 320 km. At this distance SPP will pass through the upper limit of the thermosphere[12], where the net density (ρ) is between 0.8E-14 and 1.5E-14 kg/m^3. The drag force magnitude is

$$f_{\text{drag}} = \frac{c_d \; \rho A \; v^2}{2} \tag{18}$$

Where c_d is the drag coefficient (around 2-2.5), A the effective area, and v the speed of SPP relative to the atmosphere. Take A to be that of the TPS, and v from the reference trajectory is 25 km/sec. With these values and c_d of 2.5 yields a maximum atmospheric drag force between 28 and 53 μN. Although the force has significant magnitude, its effect is very brief (in contrast to the continuous acceleration of gravity and SRP).[**] Moreover, the force is only appreciable for one of the seven Venus flybys (the final flyby). Navigation has the capability to model it, but it will likely be neglected for simplicity.

VII. Force Perturbation Summary with Uncertainties

All of the described force models represent perturbations to the trajectory, and many of these would yield large accumulated state error if left unmodeled. It is therefore critical to numerically assess the maximum expected force from each source (or force difference from a nominal). Such an analysis was performed (mostly via numerical integration)[4] to produce table 3. This gives a sense of the relative size (and importance) of the various deterministic perturbations. However, it is not required to precisely model all of these forces to meet the relatively loose navigational requirements for SPP. In contrast, the stringent requirements for the Galileo mission to Jupiter made it necessary to model all perturbations above 4 μN.[13] No analogous derived requirement exists for SPP, but if it did, a significantly greater minimum bound would be expected.

Table 3: Maximum non-gravitational force perturbations

Model	Maximum force
TPS SRP	0.016 N
Solar panels SRP	15 μN
Bus plates SRP (x-plate in full Sun at 0.7 AU)	9.9 μN
TPS SRP aberration difference	7 μN
Thermal radiators (symmetric about z axis)	15 μN
Thermal radiators z axis contribution	5.3 μN
Nominal desat (average acceleration over 0.25 AU pass)	220 μN
Outgassing	66 μN
Plasma drag	5.5 μN (radial) and 2.6 μN (along-track)
Lorentz force	1.0 nN
Atmospheric Drag	28-53 μN

Additionally, there are a number of error sources (associated with these models), which are treated as random variables. The maximum force perturbation from a 1-σ offset for each of these errors are summarized

---

[**] The position error is on the order of millimeters.

in Table 4. Of course, the importance of the various uncertainties to navigation depends on whether the errors are expected to be biased, as opposed to having zero mean. For example, a TPS misalignment would be biased, and therefore constitute a greater concern for long-term prediction compared to the mostly random uncertainty from non-radial thermal re-radiation. Non-radial SRP force perturbations (primarily due to unmodeled asymmetries) are accounted for by the G_x and G_y parameters of the S/C-bus element governed by Eq. (4).

Table 4: Non-gravitational force uncertainty bounds

Source	Maximum perturbation from 1-σ model error
Solar irradiance	1.5 mN
Spacecraft plate area	1.5 mN
penumbra irradiance and solar limb darkening	10 μN
Attitude error (SRP TPS)	11.0 μN
Attitude error (SRP solar panels)	0.7 μN
TPS misalignment (SRP TPS)	22.0 μN
Asymmetric non-radial thermal re-radiation (cooling system)	0.096 μN
Perfectly correlated desat ΔV error (during 0.25 AU pass)	51 μN
Desat frequency uncertainty	19.8 μN
Plasma drag uncertainty	0.5 μN
Atmospheric density uncertainty	10 μN

VIII. Measurement corrections due to solar plasma

It is well known that radiometric data can be affected by the charged particles in the solar plasma and solar wind.[14,15] Charged particles advance the signal phase, erroneously indicating a transmission speed faster than light. The result is that range modulations are delayed, and carrier phase is advanced. The path delay is proportional to the integral of the charged particle density along the line of sight.[15] Hence, the delay is greatest at low Sun-Earth-probe (SEP) angle (where density along the path is high). The delay is pronounced for SPP, due to its frequent proximity to the Sun and substantial time spent at low SEP.

Moreover, the plasma introduces a "non-white" phase noise power spectrum to Doppler observables, which is particularly dominant at low SEP.[16] The observations need to be transformed, to remove measurement correlations prior to weighting the data at the mean-square value of the Doppler residuals (as is typical practice). Alternately, data may be weighted appropriately as a function of SEP and the measurement reference frequency.[15,17]

A. Path delay

Ref. 14 (section 10.4) outlines an implementation for correcting the path delay during the light-time computation of radiometric observables. The correction is positive for two-way range observables, and significantly large (above 100 m) at low SEP.[8] It is negligible for differenced-phase Doppler observables, since the path delay is being subtracted. For radiometric data types the received carrier phase ϕ_r is given by

$$\phi_r = 2\pi f \left(t - \frac{d}{c} - \tau_{cp} \right) \tag{19}$$

where f is the carrier frequency, d the geometric distance between receiver and transmitter, c the speed of light, and τ_{cp} the the phase delay due to charged particles. The delay is given approximately by Sovers[18] as

$$\tau_{cp} = -c \ R_e \ N_e / \left(2\pi f^2\right) \tag{20}$$

where R_e is the electron radius (2.82E-15 m) and N_e the number of electrons per square meter along the signal path (which is equal to the integral of the electron density along that path). The path delay effect is not currently implemented in the MONTE software[7] used operationally at JPL. But SPP navigation will edit two-way range measurements to add the delay, where the delay is fit to a polynomial of the SEP angle, per Folkner and Kahn.[8] At greater SEP, the dominant sources of propagation path delay[19] are the Earth's troposphere and ionosphere. These are already accounted for in JPL software (see Moyer[14] section 10.2).

B. Removing correlated noise from Doppler data

Most orbit determination software, including MONTE, uses a sequential filter approach in which measurements are assumed to be uncorrelated (errors are independent random variables). Charged particles in the solar corona and solar wind introduce a correlated noise to the phase of radiometric data, which is non-white. This noise is the dominant source of phase noise at low SEP[16], and should ideally be removed prior to performing orbit determination. This can be done by determining the data noise covariance matrix $\mathbf{R}$, which is non-diagonal (correlated). If $\mathbf{R}$ is known, the whitening process is as follows:

1. The linearized observation equations are expressed in Eq. (21), where $\mathbf{y}$ are observed residuals and $\mathbf{H}$ is the matrix of observational partial derivatives with respect to the estimated parameters $\mathbf{x}$.

$$\mathbf{y} - \mathbf{H}\mathbf{x} = \epsilon \qquad E(\epsilon\epsilon^T) = \mathbf{R} \tag{21}$$

2. The triangular square root of $\mathbf{R}$ may be used to transform to uncorrelated observations[17]

$$\mathbf{V}^{-1}\mathbf{y} - \mathbf{V}^{-1}\mathbf{H}\mathbf{x} = \mathbf{V}^{-1}\epsilon \qquad \text{where} \qquad \mathbf{R} = \mathbf{V}\mathbf{V}^T \tag{22a}$$

$$\tilde{\mathbf{y}} - \tilde{\mathbf{H}}\mathbf{x} = \tilde{\epsilon} \tag{22b}$$

   This transformation ensures that $E(\tilde{\epsilon}\tilde{\epsilon}^T)$ is diagonal.

The noise power spectrum from charged particles is shown by Folkner[15] to vary as $f^{-8/3}$. Based on this power spectrum, Mackenzie and Folkner[17] derive the Doppler autocorrelation function, and integrate to obtain a scaled data correlation function for Doppler $U_{\dot{\phi}}$

$$U_{\dot{\phi}}(\tau) = \frac{-2\tau^{a-1} + |\tau + t_c|^{a-1} + |\tau - t_c|^{a-1}}{2t_c^{a-1}} \qquad U_{ij} = U_{\dot{\phi}}(t_j - t_i) \tag{23}$$

where τ is the time between t_i and t_j (the i and j measurements in $\mathbf{y}$), t_c is the Doppler count time in seconds, and a is the exponent governing the phase noise power spectrum (assumed to be 8/3). For the unscaled matrix $\mathbf{R}$, the observation root-mean-square (RMS) value σ_{obs} for a batch of Doppler residuals is computed, and then the covariance is formed

$$R_{ij} = \sigma_{\text{obs}}^2 \, U_{\dot{\phi}}(t_j - t_i) \tag{24}$$

Note this yields diagonal terms of σ_{obs}^2 (i.e. when $i = j$). This whitening operation is currently being added to JPL navigation software.

IX. Conclusions

Venturing to a new cosmic environment necessitated a reevaluation of common assumptions in interplanetary navigation. Perhaps unsurprisingly, the importance of solar radiation pressure is magnified on this mission, but details such as aberration and solar limb darkening are generally neglected by navigation. Other aspects are more subtle, such as having autonomous desats with uncertain frequency. This element of the spacecraft operational design is largely a function of large (and uncertain) solar pressure torque and limited communication coverage at low solar range. Continuing challenges include how to accurately model solar panel shadowing without a substantial increase in the trajectory integration time, and in properly treating the uncertainty in desat event frequency. Nevertheless, this paper provides navigation's current-best-estimate for non-gravitational modeling assumptions. SPP is entering an unexplored frontier, and undoubtedly some modeling will be revised with operational experience.

Acknowledgments

This work was carried out at the Jet Propulsion Laboratory, California Institute of Technology, under a contract with the National Aeronautics and Space Administration. Copyright 2016 California Institute of Technology. U.S. Government sponsorship acknowledged.

References

[1] Fox, N., Velli, M., Bale, S., Decker, R., Driesman, A., Howard, R., Kasper, J., Kinnison, J., Kusterer, M., Lario, D., Lockwood, M., McComas, D., Raouafi, N., and Szabo, A., "The Solar Probe Plus Mission: Humanity's First Visit to Our Star," *Space Science Reviews*, 2015, pp. 1–42.

[2] Guo, Y., McAdams, J., Ozimek, M., and Shyong, W.-J., "Solar Probe Plus Mission Design Overview and Mission Profile," *24th International Symposium on Space Flight Dynamics (ISSFD), Laurel, Maryland*, May 5-9 2014.

[3] Georgevic, R., "Mathematical model of the solar radiation force and torques acting on the components of a spacecraft," Tech. rep., JPL technical memorandum 33-494, 1971.

[4] Jones, D. R., "Solar Probe Plus (SPP) Non-Radial Accelerations," *JPL IOM 392A-16-001 (internal document)*, January 2016.

[5] Guo, Y., Shyong, W.-J., and Scott, C. J., "Solar Radiation Pressure Modeling in Mission Design Software for Solar Probe Plus," *SEG-13-004 (internal document)*, January 2013.

[6] Moller, C., *The Theory of Relativity*, Oxford, 1972.

[7] Evans, S., Taber, W., Drain, T., Smith, J., Wu, H.-c., Guevara, M., Sunseri, R., and Evans, J., "MONTE: The Next Generation of Mission Design & Navigation Software," *The 6th International Conference on Astrodynamics Tools and Techniques*, 2016.

[8] Folkner, W. M. and Kahn, R. D., "Nominal Solar Plasma Model," *JPL IOM 335.1-92-39 (internal document)*, December 1992.

[9] Schwenn, R., "Solar Wind: Global Properties," *Encyclopedia of Astronomy and Astrophysics*, 2005.

[10] Coles, W. A. and Harmon, J. K., "Propagation observations of the solar wind near the sun," *Astrophysical Journal, Part 1 (ISSN 0004-637X)*, Vol. 337, Feb. 1989, pp. 1023–1034.

[11] Gopalswamy, N. and Yashiro, S., "The Strength and Radial Profile of Coronal Magnetic Field from the Standoff Distance of a CME-driven Shock," *arXiv*, Vol. 1106, No. 4832, 2011.

[12] Justh, H., Justus, J., and Keller, V., "Global Reference Atmospheric Models, including Thermospheres for Mars, Venus, and Earth," *AIAA/AAS Astrodynamics Specialist Conference*, 2006.

[13] Longuski, J., Todd, R., and Konig, W., "Survey of Nongravitational Forces and Space Environmental Torques: Applied to the Galileo," *Journal of Guidance, Control, and Dynamics*, Vol. 15, No. 3, 1992, pp. 545–553.

[14] Moyer, T. D., *Formulation for Observed and Computed Values of Deep Space Network Data Types for Navigation*, Vol. 3, John Wiley and Sons, 2005.

[15] Folkner, W. M., "Effect of Uncalibrated Charged Particles on Doppler Tracking," *JPL IOM 335.1-94-005 (internal document)*, March 1994.

[16] Asmar, S., Armstrong, J., Iess, L., and Tortora, P., "Spacecraft Doppler tracking: Noise budget and accuracy achievable in precision radio science observations," *Radio Science*, Vol. 40, 2005.

[17] Mackenzie, R. and Folkner, W. M., "Applying Appropriate Weights to Doppler data," *JPL IOM 343J-06-034 (internal document)*, October 2006.

[18] Sovers, O., "Observation model and parameter partials for the JPL VLBI parameter estimation software MODEST," Tech. rep., Jet Propulsion Laboratory, 1991.

[19] Standish, E., "The observational basis for JPL's DE 200, the planetary ephemerides of the Astronautical Almanac," *Astronomy and Astrophysics*, Vol. 233, 1990, pp. 252–271.